PHYSICAL REVIEW B **75**, 214409 (2007)

Phase diagram and spin Hamiltonian of weakly-coupled anisotropic $S=\frac{1}{2}$ chains in $CuCl_2 \cdot 2((CD_3)_2SO)$

Y. Chen,[1,2] M. B. Stone,[1,3] M. Kenzelmann,[1,4] C. D. Batista,[5] D. H. Reich,[1] and C. Broholm[1,2]

[1]*Department of Physics and Astronomy, Johns Hopkins University, Baltimore, Maryland 21218, USA*

[2]*NIST Center for Neutron Research, National Institute of Standards and Technology, Gaithersburg, Maryland 20899, USA*

[3]*Neutron Scattering Science Division, Oak Ridge National Laboratory, Oak Ridge, Tennessee 37831, USA*

[4]*Laboratory for Solid State Physics, ETH Zurich, CH-8093 Zurich, Switzerland*

[5]*Theoretical Division, Los Alamos National Laboratory, Los Alamos, New Mexico 87545, USA*

(Received 11 January 2007; revised manuscript received 4 March 2007; published 5 June 2007)

Field-dependent specific heat and neutron scattering measurements were used to explore the antiferromagnetic $S=\frac{1}{2}$ chain compound $CuCl_2 \cdot 2((CD_3)_2SO)$. At zero field the system acquires magnetic long-range order below $T_N=0.93$ K with an ordered moment of $0.44\mu_B$. An external field along the **b** axis strengthens the zero-field magnetic order, while fields along the **a** and **c** axes lead to a collapse of the exchange stabilized order at $\mu_0 H_c=6$ T and $\mu_0 H_c=4$ T (extrapolated to zero temperature) and the formation of an energy gap in the excitation spectrum. We relate the field-induced gap to the presence of a staggered g-tensor and Dzyaloshinskii-Moriya interactions, which lead to effective staggered fields for magnetic fields applied along the **a** and **c** axes. Competition between anisotropy, interchain interactions, and staggered fields leads to a succession of three phases as a function of field applied along the **c** axis. For fields greater than $\mu_0 H_c$, we find a magnetic structure that reflects the symmetry of the staggered fields. The critical exponent, β, of the temperature driven phase transitions are indistinguishable from those of the three-dimensional Heisenberg magnet, while measurements for transitions driven by quantum fluctuations produce larger values of β.

DOI: 10.1103/PhysRevB.75.214409 PACS number(s): 75.25.+z, 75.10.Pq, 74.72.−h

I. INTRODUCTION

Weakly-coupled antiferromagnetic (AF) spin $S=\frac{1}{2}$ chains can be close to one or several quantum critical points and serve as interesting model systems in which to explore strongly-correlated quantum order. An isolated AF $S=\frac{1}{2}$ Heisenberg chain, described by

$$\mathcal{H} = J\sum_n \mathbf{S}_n \cdot \mathbf{S}_{n+1}, \tag{1}$$

is quantum critical at zero temperature. Due to the absence of a length scale at a critical point, the spin correlations decay as a power law, and the fundamental excitations are fractional spin excitations called spinons that carry $S=\frac{1}{2}$.[1,2] Interactions that break the symmetry of the ground state can induce transitions to ground states of distinctly different symmetry, such as one-dimensional long-range order at zero temperature in the presence of an Ising anisotropy or conventional three-dimensional long-range order at finite temperature in the presence of weak nonfrustrating interchain interactions.[3]

Magnetic fields break spin rotational symmetry and allow tuning the spin Hamiltonian in a controlled way. When it couples identically to all sites in a spin chain, an external field uniformly magnetizes the chain and leads to gapless excitations that are incommensurate with the lattice. Experimentally this is observed with methods that couple directly to the spin correlation functions, such as neutron scattering. Inelastic neutron scattering experiments on model AF $S=\frac{1}{2}$ chain systems such as copper pyrazine dinitrate[4] show that upon application of a uniform magnetic field there are gapless excitations at an incommensurate wave vector that moves across the Brillouin zone with increasing field.[5] This is expected to be a rather general feature of a partially magnetized quantum spin system without long-range spin order at $T=0$ K. However, when even and odd sites of the spin chain experience different effective fields, there is an entirely different ground state which is separated by a finite gap from excited states. This has been observed in magnetic materials[6–9] with staggered crystal field environments and Dzyaloshinskii-Moriya (DM) interactions. Most notably, the generation of an excitation energy gap was first observed in copper benzoate using neutron scattering[6] and the entire excitation spectrum of the $S=\frac{1}{2}$ chain in the presence of an effective staggered field was mapped out in $CuCl_2 \cdot 2DMSO$ (CDC).[9] These experiments showed that the excitation spectrum in high staggered fields consists of solitons and breathers that can be described as bound spinon states, and that the one-dimensional character of the spinon potential leads to high-energy excitations that are not present in the absence of staggered fields.[10]

In this paper, we explore the strongly anisotropic field dependence of long-range magnetic order in CDC. Using neutron scattering, we have directly measured the order parameters associated with the various competing phases. We show that a magnetic field destroys the low-field long-range order that is induced by superexchange interactions involving Cl^- cations, and that an applied field induces a first-order spin-flop transition followed by a second-order quantum phase transition. Field-dependent specific heat measurements provide evidence for a gapless excitation spectrum in the low-field phase and an energy gap for larger fields. These results combined with neutron measurements enable a comprehensive characterization of the dominant spin interactions in this system, including a quantitative determination of the staggered gyromagnetic tensor and the DM interactions, which give rise to the field-induced gap.

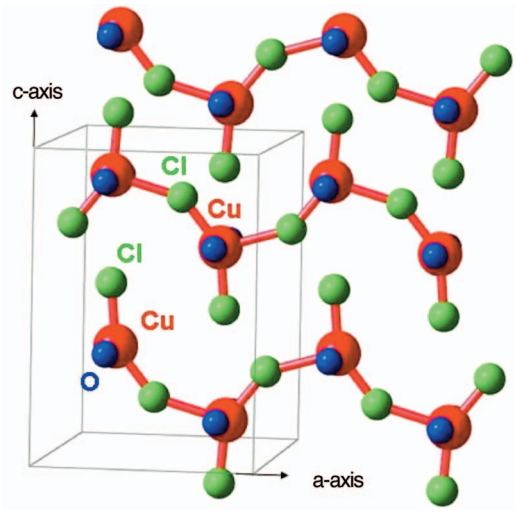

FIG. 1. (Color) Position of Cu^{2+} (red), Cl^{-} (green), and O^{-} (blue) in the crystal structure of CDC. The dominant superexchange interactions are via Cu^{2+}-Cl^{-}-Cu^{2+} paths forming linear chains along the **a** axis. The axes of the quasiplanar $CuCl_2O_2$ groups alternates by 22° along the chain direction, leading to a staggered gyromagnetic tensor **g**.

II. CRYSTAL STRUCTURE

CDC crystallizes in the orthorhombic space group *Pnma* (No. 62) with room-temperature lattice constants $a=8.054$ Å, $b=11.546$ Å, and $c=11.367$ Å.[11] Based on the temperature dependence of the magnetic susceptibility, CDC was proposed as an AF $S=\frac{1}{2}$ chain with exchange constant $J=1.43$ meV.[12] Inspection of the crystal structure (the positions of the Cu^{2+} sublattice are given in Appendix A) suggests strong superexchange interactions between Cu^{2+} ions via Cl^{-} cations, so that the Cu^{2+} ions form spin chains along the **a** axis, as shown in Fig. 1. Inelastic neutron scattering measurements described below yield a consistent value of $J=1.46$ meV.

The local symmetry axis of the Cl^{-} environment lies entirely in the *ac* plane, but alternates its orientation along the **a** axis. This alternation of the local crystalline environment leads to an alternating **g** tensor in CDC of the following form:

$$\mathbf{g}_n = \begin{pmatrix} 2.31 & 0 & (-1)^n g^s \\ 0 & 2.02 & 0 \\ (-1)^n g^s & 0 & 2.14 \end{pmatrix} = \mathbf{g^u} + (-1)^n \mathbf{g^s}, \quad (2)$$

where n denotes the nth spin in the chains along the **a** direction.[12] $\mathbf{g^u}$ is the uniform and $\mathbf{g^s}$ is the staggered part of the **g** factor.

The crystal symmetry also allows DM interactions[13,14]

$$\mathcal{H}_{\mathrm{DM}} = \sum_n \mathbf{D}_n \cdot (\mathbf{S}_{n-1} \times \mathbf{S}_n). \quad (3)$$

The DM vector $\mathbf{D}_n=(-1)^n D\hat{\mathbf{b}}$ alternates from one chain site to the next as can be seen from the space group symmetry: First, the structure is invariant under a translation along the **a** axis by two Cu sites, meaning that there can be at most two distinct DM vectors. Second, the *ac* plane is a mirror plane, implying that the DM vectors point along the **b** axis. Third, the crystal structure is invariant under the combined operation of translation by one Cu site along the chain, and reflection in the *ab* plane.

It was shown that alternating DM interactions can result in an effective staggered field $\mathbf{H}_{\mathrm{st}}$ upon application of a uniform external field **H** (Ref. 15). Taking into account also the staggered **g** tensor, the effective staggered field that is generated by a uniform field can be written as

$$\mathbf{g^u H}_{\mathrm{st}} = \frac{1}{2J}\mathbf{D} \times \mathbf{g^u H} + \mathbf{g^s H}. \quad (4)$$

III. EXPERIMENTAL TECHNIQUES

Single crystals of CDC were obtained by slow cooling of saturated methanol solutions of anhydrous $CuCl_2$ and dimethyl sulphoxide in a 1:2 molar ratio from $T=50$ °C to 20 °C. Emerald-green crystals grow as large tabular plates with well developed (001) faces. Specific heat measurements were performed on small, protonated crystals with a typical mass of 15 mg in a dilution refrigerator, using relaxation calorimetry in magnetic fields up to 9 T applied along the three principal crystallographic directions. Measurements were performed in six different magnetic fields applied along the **a** and **b** axes, and eight different fields applied along the **c** axis.

Neutron diffraction measurements were performed on deuterated single crystals of mass 1 g using the SPINS spectrometer at the NIST Center for Neutron Research. Inelastic neutron scattering experiments were performed on multiple coaligned single crystals with a total mass of 7.76 g using the DCS spectrometer at NIST. The SPINS spectrometer was configured with horizontal beam collimations $45'/k_i$ (^{58}Ni guide)-80′-80′-300′. A pyrolytic graphite (PG) monochromator was used to select incident neutron energies of either $E_i=3$ meV, 5 meV [using the (0, 0, 2) reflection] or 20 meV [using the (0, 0, 4) reflection]. For $E_i=3$ meV and 5 meV a cooled Be filter was used before the sample to eliminate contamination from higher-order monochromator Bragg reflections. The DCS measurements were performed with an incident energy $E_i=4.64$ meV and an angle of 60° between the incident beam and the **a** axis, as detailed in Ref. 9.

IV. SPECIFIC HEAT MEASUREMENTS

The temperature dependence of the specific heat at low fields has a well-defined peak for all field directions, as shown in Fig. 2. The peak position varies with field strength and direction, all of which suggests that the peak corresponds to the onset of long-range magnetic order. At zero field, the transition temperature is $T_N=0.93$ K, in agreement with prior zero-field heat capacity measurements.[16] When the field is applied in the mirror plane, either along the **a** or the **c** axis, the Neél temperature T_N decreases with increasing field, as shown in Fig. 2(a) and Fig. 2(c). The peak becomes unobservable above $\mu_0 H_c=5.7$ T and $\mu_0 H_c=3.9$ T for fields applied along the **a** and **c** axis, respectively. At higher fields,

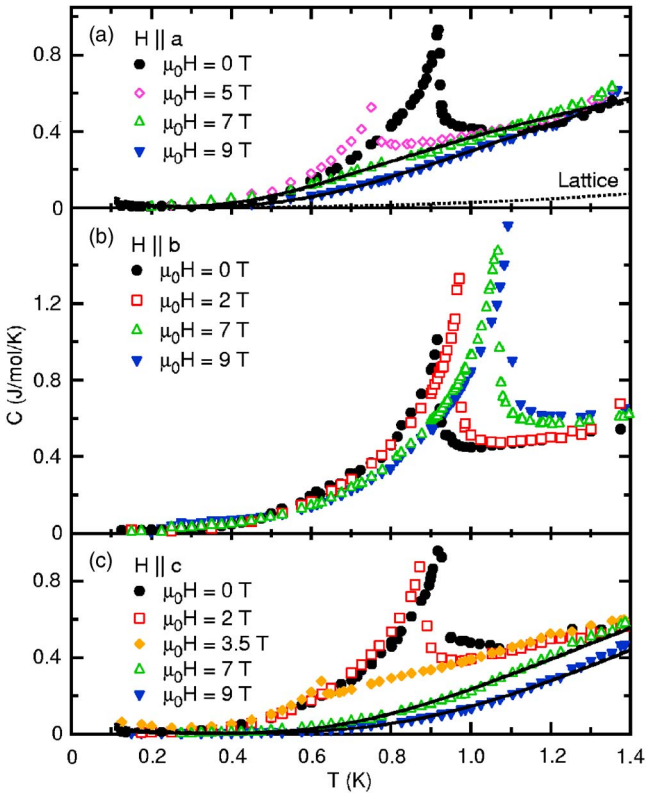

FIG. 2. (Color online) Specific heat of CDC as a function of temperature for magnetic field applied along the **a**, **b**, and **c** axis. The peaks in the temperature dependence correspond to the onset of long-range magnetic order. The solid (and the mostly hidden dashed) line corresponds to the low-temperature specific heat calculated in the framework of the sine-Gordon (boson) model and described in Eq. (10) [Eq. (6)]. The dotted line plotted in (a) corresponds to aT^3 lattice contribution to the specific heat.

the specific heat is exponentially activated, with spectral weight shifting to higher temperatures with increasing field. This is evidence for a spin gap for magnetic fields along the **a** and **c** axes. In contrast, a magnetic field along the **b** axis enhances the magnetic order and the Neél temperature increases with increasing field strength, as shown in Fig. 2(b).

We analyze the specific heat for $H > H_c$ to determine the field dependence of the spin gap. The low-temperature specific heat is first compared to a simple model (which we refer to as the *boson model*) of $\tilde{n}$ species of one-dimensional noninteracting gapped bosons with a dispersion relation

$$\hbar\omega(\tilde{q}) = \sqrt{\Delta^2 + [v(\tilde{q} - \tilde{q}_0)]^2}. \tag{5}$$

Here Δ is the spin gap, v is the spin-wave velocity, which depends on both the strength and orientation of the magnetic field, $\tilde{q}$ is the chain wave vector $\tilde{q} = \pi h$ and $\tilde{q}_0 = \pi$. The specific heat of a one-dimensional boson gas in this boson model is given by[17]

$$C_{\mathrm{mag}}(T) = \frac{\tilde{n}R}{\sqrt{2\pi}}\left(\frac{\Delta}{k_B T}\right)^{3/2}\frac{\Delta}{v}\exp(-\Delta/k_B T). \tag{6}$$

Terms proportional to $\frac{H^2}{T^2}$ and to T^3 were included in the fit to take into account the small nuclear spin and lattice contributions, respectively. The total function fitted to the specific heat was

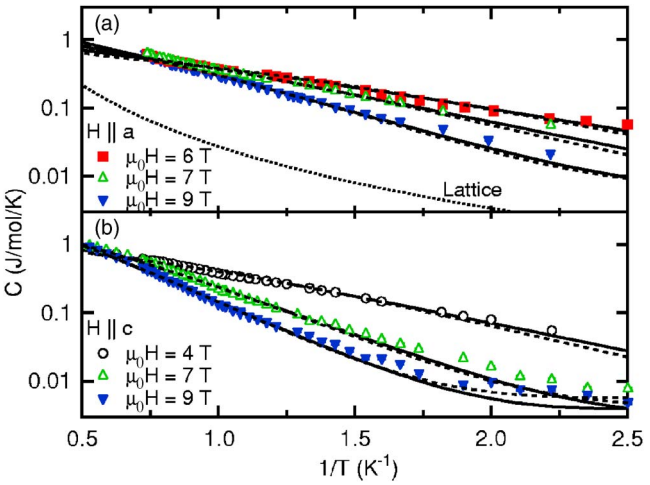

FIG. 3. (Color online) Semilogarithmic plot of the specific heat $C(H,T)$ in the high-field gapped phase as a function of the inverse temperature $1/T$ for different magnetic fields applied along the (a) **a** and (b) **c** axes, respectively. The solid (dashed) line corresponds to the low-temperature specific heat calculated in the framework of the sine-Gordon (boson) model and is given in Eq. (10) [Eq. (6)]. The dotted line plotted in (a) corresponds to aT^3 lattice contribution to the specific heat.

$$C(T,H) = C_{\mathrm{mag}} + aT^3 + b(H/T)^2. \tag{7}$$

All data for $T < \Delta$ and $H > H_c$ were fit simultaneously to Eq. (7), yielding $a = 0.027(1)$ J/mol K^4 and $b = 8(2) \times 10^{-6}$ J mol K/T^2. The average spin-wave velocity is found to be $v/\tilde{n} = 0.65(1)$ and $0.58(2)$ meV/mode for fields along the **a** and **c** axis, respectively. From our previous measurements of the field-induced incommensurate mode[10] we found that the spin-wave velocity is $v = 1.84(4)$ meV. This yields $\tilde{n} = 2.8$ for the number of gapped low-energy modes which contribute to the specific heat, in excellent agreement with the expectation of one longitudinal and two transverse modes. The resulting field and orientation dependent spin gaps are shown in Fig. 4, and the calculated $C(T,H)$ for the boson model are plotted as dashed lines in Figs. 2 and 3.

We also analyze the specific heat in the framework of the sine-Gordon model, to which the Hamiltonian can be mapped in the long wavelength limit.[15] The sine-Gordon model is exactly solvable, with solutions that include massive soliton and breather excitations. The soliton mass, M, is given by[18,19]

$$M \approx J\left(\frac{g\mu_B H_{\mathrm{st}}}{J}\right)^{(1+\xi)/2} \times \left[B\left(\frac{J}{g\mu_B H}\right)^{(2\pi-\beta^2)/4\pi}\left(2 - \frac{\beta^2}{\pi}\right)^{1/4}\right]^{-(1+\xi)/2}. \tag{8}$$

Here $\xi = \beta^2/(8\pi - \beta^2) \to 1/3$ for $\mu_0 H \to 0$, $B = 0.422\,169$, and $\mu_0 H_{\mathrm{st}}$ is the effective staggered field. The mass of the breathers, M_n, is given by

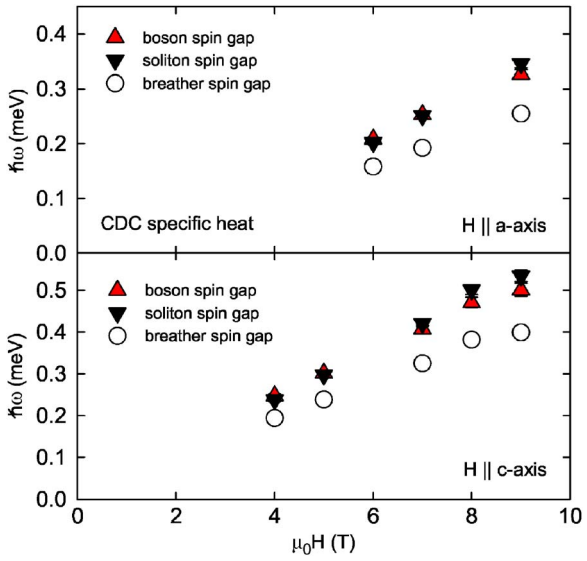

FIG. 4. (Color online) Field dependence of the energy gaps for the boson and sine-Gordon models, derived from fits to specific heat data as shown in Fig. 3. The error bars are smaller than the symbol size.

$$M_n = 2M \sin(n\pi\xi/2), \tag{9}$$

where $1 \leqslant n \leqslant [1/\xi]$ with ξ depending entirely on the applied field.[20] The temperature dependence of the specific heat due to breathers and solitons is given by[21]

$$C \sim \sum_{\alpha=0}^{[1/\xi]} \frac{(1+\delta_{\alpha 0})M_\alpha}{\sqrt{2\pi v}}\left[1+\frac{k_B T}{M_\alpha}+\frac{3}{4}\left(\frac{k_B T}{M_\alpha}\right)^2\right] \times \left(\frac{M_\alpha}{k_B T}\right)^{3/2} \exp\left(-\frac{M_\alpha}{k_B T}\right), \tag{10}$$

where $M_0 \equiv M$. We use this expression for an additional comparison to the experimentally observed temperature and field dependence of the specific heat $C(T,H)$ for $T < M_1$ and $H > H_c$, in order to determine the soliton mass as a function of field strength and orientation. These results are shown as solid lines in Figs. 2 and 3. The adjusted soliton and breathers masses are shown in Fig. 4, in comparison with the results from the boson model.

The adjusted boson mass is larger than the breather mass, but smaller than the soliton mass, as expected from a model which is only sensitive to an average gap energy. The soliton energy is different for fields applied along the **a** and **c** axis as a result of different staggered fields arising from the staggered g factor and DM interactions.

The field dependence of the gap for two different field directions allows an estimate of the strength of g_s and D/J. The best estimate is obtained for high fields where the effect of the low-field ordered phase is small. Assuming $H_{st}=cH$ and fitting Eq. (8) to the field dependence of the gap, we obtain $c=0.045(2)$ for fields along the **a** axis and $c=0.090(4)$ for fields along the **c** axis. Comparing these results with Eq. (4) we obtain

$$g^s - g^{aa}D/2J = 0.045,$$

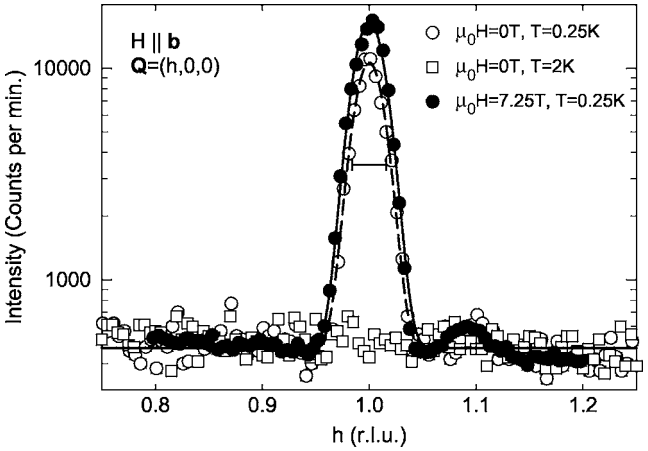

FIG. 5. $(h,0,0)$ scans through $\mathbf{Q}=(1,0,0)$ magnetic Bragg peak in CDC at $T=0.25$ K, $\mu_0 H=7.25$ T$\|\mathbf{b}$, $T=0.25$ K, and $T=2$ K at zero field. The bar in the figure represents the calculated peak width of $\mathbf{Q}=(1,0,0)$ based on the known instrumental resolution. The peak at $h=1.09$ appears to be field and temperature independent indicating that it does not arise from magnetic scattering.

$$g^s + g^{cc}D/2J = 0.09. \tag{11}$$

With $g^{aa}=2.28$ and $g^{cc}=2.12$ (Ref. 12), this leads to $g^s=0.068(3)$ and $D/J=0.0102(5)$, establishing the presence of both small DM interactions and a staggered g factor in CDC. The DM interactions in CDC are considerably smaller than in copper pyrimidine dinitrate where $D/J=0.139$ (Ref. 7) and in copper benzoate where $D/J=0.131$ (Ref. 15).

V. NEUTRON DIFFRACTION

Neutron diffraction measurements were performed in the $(h,0,l)$ and $(h,k,0)$ reciprocal lattice planes. Figure 5 shows h scans through the (1, 0, 0) reflection for different temperatures and fields. At zero field and $T=0.3$ K a resolution-limited peak is observed at $h=1$. The peak is absent for temperatures higher than $T_N=0.93$ K. No incommensurate order was observed in any of our experiments. The reflections we found can be indexed by $(2n,m,0)$ in the $(h,k,0)$ plane, whereas magnetic diffraction was found only at the (1, 0, 0) and the (3, 0, 0) reciprocal lattice points in the $(h,0,l)$ plane for $|\mathbf{Q}| < 2.6$ Å^{-1}.

A. HT-phase diagram

The phase diagram of CDC was explored further with neutron diffraction for fields up to 7.25 T, applied along the **b** and **c** axes. Figure 6 summarizes the magnetic field dependence of elastic scattering measurements at the (1, 0, 0) wave vector. Applying a field along the **b** axis increases the intensity of the (1, 0, 0) reflection and we associate this with an increase in the staggered magnetization. In contrast, a field along the **c** axis decreases the intensity of the (1, 0, 0) Bragg peak, first in a sharp drop at 0.3 T suggestive of a spin-flop transition, and then in a continuous decrease towards a second phase transition at 3.9 T. The transition at 3.9 T is evidence that exchange-induced long-range order is suppressed

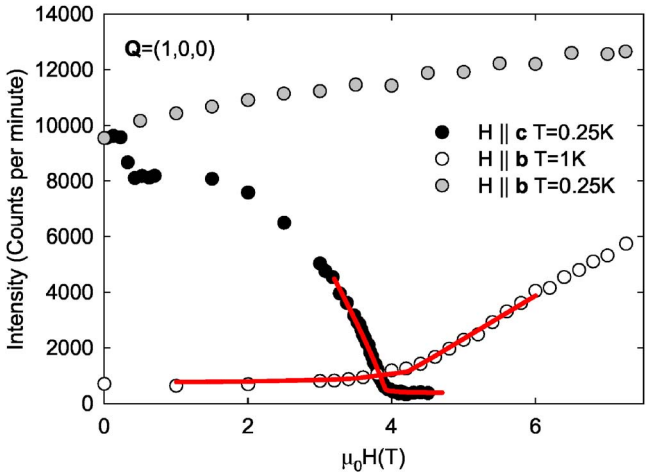

FIG. 6. (Color online) Measured field dependence of the **Q** =(1,0,0) magnetic peak intensity at T=0.25 K with the field applied along the **c** axis, and at T=0.25 K and at T=1 K with the field applied along the **b** axis. The solid lines represent the fits explained in Sec. V C.

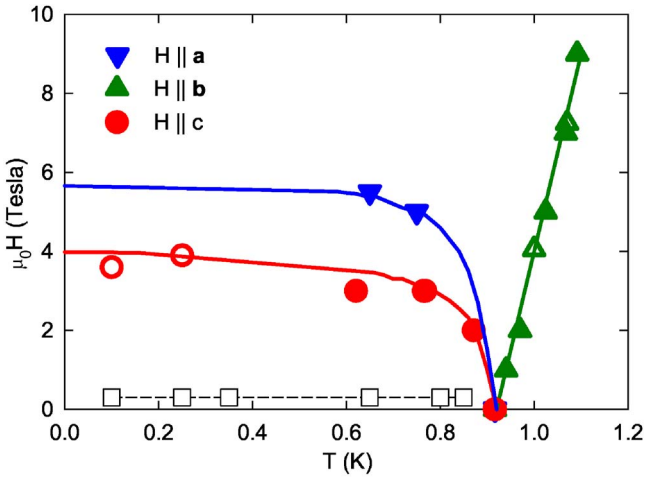

FIG. 8. (Color online) Field-temperature phase diagram of CDC determined from heat capacity measurements (filled symbols) and from neutron scattering (open symbols). The squares indicate the spin-flop transition observed for a field along the **c** axis. The solid and dashed lines are a guide to the eye.

by the application of fields along the **c** axis. The value of the critical field, 3.9 T, is in agreement with specific heat measurements.

Figure 7 shows the temperature dependence of the (1, 0, 0) magnetic Bragg peak for fields applied along the **b** and **c** axis. For fields along the **b** axis, the Bragg peak has higher intensity at low T and the enhanced intensity survives to higher temperatures than in the zero-field measurement. For fields along the **c** axis, the intensity is reduced and the transition temperature is lower than at zero field. The phase transition remains continuous, regardless of the direction of the field.

The phase diagram in Fig. 8 shows a synopsis of the results obtained from specific heat and neutron diffraction measurements. CDC adopts long-range magnetic order below T_N=0.93 K. This order can be strengthened by the application of a magnetic field along the **b** axis, which enhances the ordered moment and increases the transition temperature to long-range order. In contrast, applying fields along the **a** and **c** axes competes with the zero-field long-range order, decreasing the critical temperature, and leading eventually to the collapse of the low-field long-range order at 6 and 4 T, respectively, as extrapolated to zero temperature.

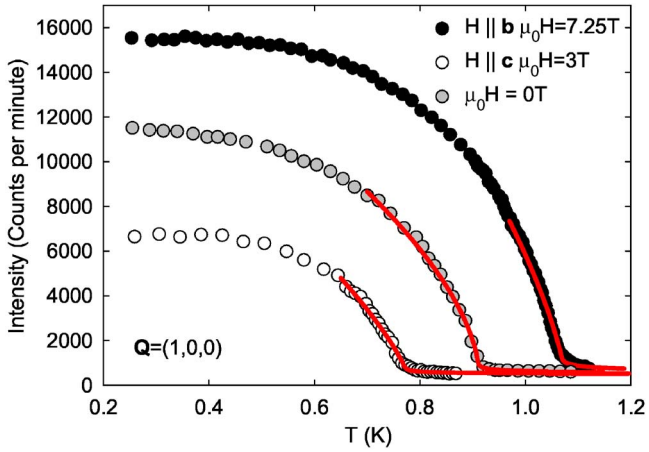

FIG. 7. (Color online) Measured temperature dependence of the **Q**=(1,0,0) magnetic peak intensity for zero field, $\mu_0 H$=7.25 T applied parallel to the **b** axis and $\mu_0 H$=3 T applied parallel to the **c** axis. The solid lines represent the fits explained in Sec. V C.

B. Magnetic structures

To understand the field-induced phase transitions, it is important to determine the symmetry of the magnetic structures below and above the transitions. The intensities of ~40 magnetic Bragg peaks were measured at 0.1 K at zero field, at $\mu_0 H$=0.5 T, and at 10 T applied along the **c** axis. The ordering wave vector for both structures is **k**=(0,0,0). We use group theory to identify the spin configurations consistent with the wave vector **k** for the given crystal symmetry, and compare the structure factor of possible spin configurations with the observed magnetic Bragg peak intensities. The group theoretical analysis which leads to the determination of the symmetry allowed basis vectors is presented in Appendix B.

At zero field and T=0.1 K, best agreement [see Table I and Figs. 10(a) and 10(b)] with the experiment is obtained for a magnetic structure belonging to representation Γ^2 as defined in Appendix B with χ^2=3.1 and R=0.43. The magnetic structure is collinear with a moment of 0.44(5)μ_B along the **c** axis as shown in Fig. 9(a). The alignment of the moment along the **c** axis suggests an easy-axis anisotropy along this direction, which is not included in the zero-field Hamiltonian defined by Eq. (1). The ordered magnetic moment is significantly less than the free-ion moment, as expected for a system of weakly-coupled $S=\frac{1}{2}$ chains close to a quantum critical point.[22]

At $\mu_0 H$=0.75 T after the system undergoes a spin-flop transition, the magnetic order can be described by the representation Γ^5 with χ^2=1.75 and R=0.49 [Table II and Fig.

TABLE I. Measured magnetic Bragg peak intensities at $\mu_0 H = 0$ T, compared with the best fit with $\chi^2 = 3.1$ and $R = 0.43$. The derived magnetic structure belongs to Γ^2 and the moment is aligned along the z axis. The next best fit yields a magnetic structure that belongs to Γ^5 with the magnetic moments aligned along the y axis, with $\chi^2 = 5.2$ and $R = 0.67$.

(h,k,l)	I_{exp}	I_{cal}
(−1,7,0)	−4 (2)	1.38
(−1,8,0)	0 (2)	3.43
(0, 3, 0)	0 (2)	0
(0, 7, 0)	0 (2)	0
(3, 4, 0)	1 (2)	0.722
(3, 2, 0)	3 (2)	1.12
(5, 1, 0)	3 (2)	4.17
(3, 5, 0)	4 (2)	9.11
(5, 2, 0)	5 (2)	2.21
(3, 7, 0)	5 (2)	3.7
(3, 6, 0)	5 (2)	0.344
(−1,5,0)	5 (2)	3.32
(5, 3, 0)	5 (2)	3.09
(1, 8, 0)	5 (2)	3.43
(1, 7, 0)	5 (2)	1.38
(1, 5, 0)	5 (2)	3.32
(1, 3, 0)	6 (2)	6.55
(5,−1,0)	7 (2)	4.17
(−1,6,0)	7 (2)	9.76
(−1,3,0)	8 (2)	6.55
(1, 6, 0)	8 (2)	9.76
(5, 0, 0)	11 (2)	2.57

10(c)]. Slightly lower values for χ^2 are obtained if a small antiferromagnetic moment belonging to Γ^8 is also allowed for. As shown in Fig. 9(b), the spin structure is collinear with a magnetic moment of $0.3(1)\mu_B$ per Cu^{2+} along the **b** axis (and perpendicular to the field as expected for a spin-flop transition).

At $\mu_0 H = 10$ T, the magnetic order can be described by representation Γ^8 with $\chi^2 = 2.41$ and $R = 0.21$ (Table III and Fig. 10). The spin structure is a canted magnetic structure where the magnetic moments along the **a** axis point along the staggered fields in the material, as shown in Fig. 9(c). The antiferromagnetically ordered moment along the **a** axis is $0.49(5)\mu_B$ per Cu^{2+}. Our numerical calculations[10] using a the Lanczos method for finite chains of 24 sites yield a ordered staggered moment $0.55\mu_B$ per site, in good agreement with the experiment.

The magnetic structures reveal why fields along the **a** and **c** axis lead to the collapse of long-range order, while a field along the **b** axis strengthens magnetic order. A field along the **c** axis leads to staggered fields due to the alternating g tensor and DM interactions, as illustrated in Fig. 9(d). These staggered fields compete with interchain interactions which favor a different antiferromagnetic arrangement of spins. For example, interchain exchange favors AF alignment of the neighboring magnetic moments on sites 1 and 4, but the staggered fields favor ferromagnetic alignment along the **a** axis. This must lead to an increase in quantum fluctuations which leads to a collapse of magnetic order, identifying the transition as a quantum phase transition. This situation was recently analyzed by Sato and Oshikawa.[23]

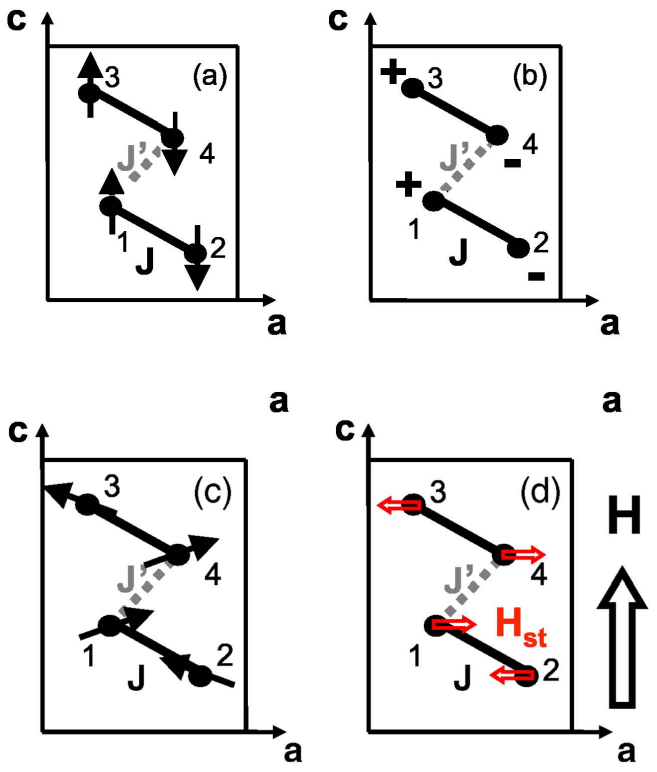

FIG. 9. (Color online) Magnetic structures at zero field (a), 0.75 T (b), and 10 T (c), with the field H applied along the **c** axis. The solid arrows indicate the spin directions, + and − indicate spins pointing into opposite directions along the **b** axis. The Cu^{2+} positions are defined in Appendix A. Because the ordering wave vector is $\mathbf{k} = (0,0,0)$, the spin arrangement in other unit cells is identical. (d) Directions of the staggered fields $\mathbf{H}_{st}$ upon application of an external field **H** along the **c** axis.

Application of a field along the **b** axis does not induce staggered fields, and so merely quenches quantum fluctuations for small field strengths, thereby leading to an enhancement of the antiferromagnetically ordered moment as observed in the experiment. Application of a field along the **a** axis should not lead to a spin-flop transition, because the moments in the zero-field structure are already perpendicular to that field direction. At higher fields, however, the competition between magnetic order arising from either spin exchange or staggered fields becomes important, leading eventually to the phase transition at $\mu_0 H = 5.7$ T into a gapped phase that is described by the sine-Gordon model.

C. Critical exponents

The neutron diffraction measurements allow determination of the order parameter critical exponent β for the phase transition to long-range order. Figure 11 shows the magnetic intensity of the (1,0,0) reflection close to the critical region.

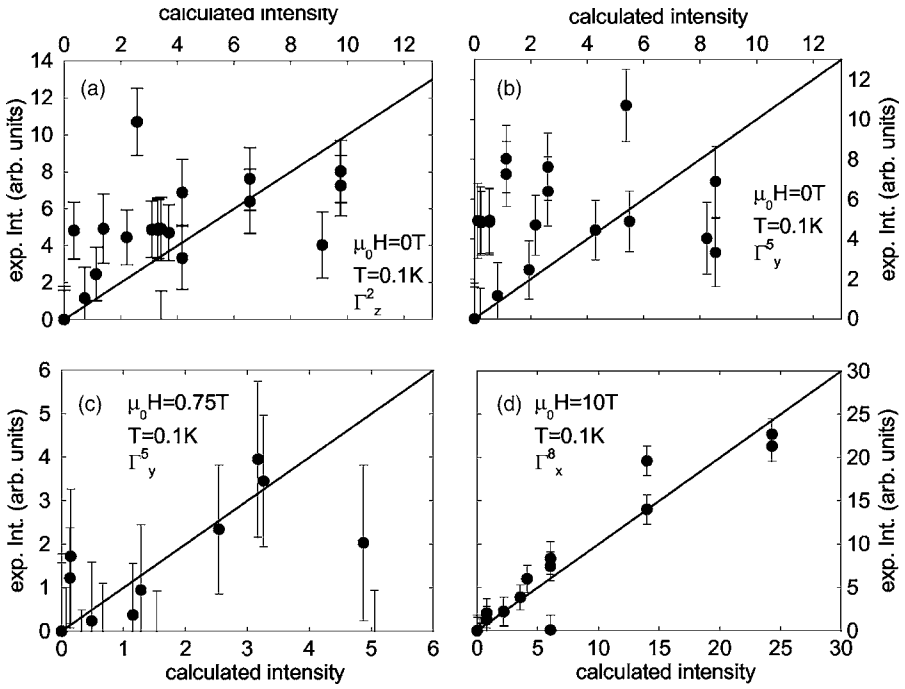

FIG. 10. (a)–(d) Observed magnetic intensities plotted as a function of calculated intensities, showing the quality of our fits. (a) and (b) compares the best fit for $\mu_0 H=0$ T with the second best fit, while (c) and (d) show the best fits for $\mu_0 H=0.75$ T and $\mu_0 H=10$ T, respectively.

The data were corrected for a nonmagnetic, constant background.

The temperature scans are shown as a function of reduced temperature $(1-T/T_c)$ for zero field, $\mu_0 H=7.25$ T applied along the **b** axis and $\mu_0 H=3$ T applied along the **c** axis. Power law fits were performed using

TABLE II. Measured magnetic Bragg peak intensities at $\mu_0 H=0.75$ T, compared with the best fit with $\chi^2=1.75$ and $R=0.49$. The derived magnetic structure belongs to Γ^5 and the moment is aligned along the y axis. The next best fit yields a magnetic structure that belongs to Γ^4 with the magnetic moments aligned along the x axis, with $\chi^2=5.3$ and $R=0.96$.

(h,k,l)	I_{exp}	I_{cal}
(1, 5, 0)	−1 (1)	0.321
(5, 1, 0)	0 (1)	5.05
(1, 7, 0)	0 (1)	0.0705
(1, 6, 0)	0 (1)	0.671
(1, 3, 0)	0 (1)	1.54
(0, 3, 0)	0 (2)	0
(0, 7, 0)	0 (2)	0
(3, 4, 0)	0 (1)	0.485
(3, 2, 0)	0 (1)	1.15
(3, 7, 0)	1 (2)	1.28
(1, 8, 0)	1 (1)	0.136
(3, 6, 0)	2 (2)	0.147
(3, 5, 0)	2 (2)	4.87
(5, 2, 0)	2 (2)	2.54
(5, 3, 0)	4 (2)	3.26
(5, 0, 0)	4 (2)	3.17

TABLE III. Measured magnetic Bragg peak intensities at $\mu_0 H=10$ T, compared with the best fit with $\chi^2=2.4$ and $R=0.21$. The derived magnetic structure belongs to Γ^8 and the moment is aligned along the x axis. The next best fit yields a magnetic structure that belongs to Γ^6 with the magnetic moments aligned along the z axis, with $\chi^2=8.2$ and $R=0.34$.

(h,k,l)	I_{exp}	I_{cal}
(5, 1, 0)	−5 (2)	0.0479
(5, 0, 0)	−3 (2)	0
(5,−1,0)	−2 (2)	0.0479
(3, 5, 0)	−1 (2)	0.308
(3, 7, 0)	−1 (2)	0.159
(5, 3, 0)	−1 (2)	0.278
(5, 2, 0)	0 (2)	0.273
(0, 3, 0)	0 (2)	0
(0, 7, 0)	0 (2)	0
(−1,7,0)	0 (2)	6.05
(−1,8,0)	1 (2)	0.792
(1, 8, 0)	2 (2)	0.792
(1, 6, 0)	2 (2)	22
(−1,6,0)	2 (2)	22
(3, 2, 0)	4 (2)	3.57
(3, 6, 0)	6 (2)	4.13
(3, 4, 0)	7 (2)	6.04
(1, 7, 0)	8 (2)	6.05
(−1,5,0)	14 (2)	14
(1, 5, 0)	20 (2)	14
(−1,3,0)	21 (2)	24.3
(1, 3, 0)	23 (2)	24.3

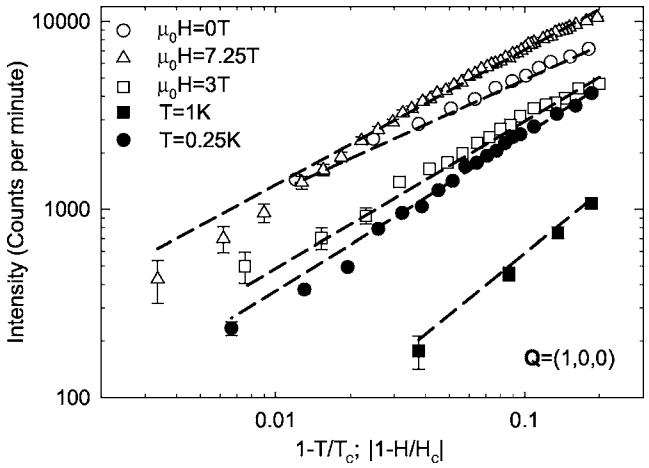

FIG. 11. Logarithmic plot of the background corrected **Q** =(1,0,0) magnetic intensity plotted as a function of reduced temperature (open symbols) or versus reduced field (filled symbols). Dashed lines corresponds to the power law fits described in the text. For the temperature scans, $\mu_0 H=7.25$ T was applied along the **b** axis, and $\mu_0 H=3$ T was applied along the **c** axis. For the field scans at constant temperature, the field was applied along the **b** axis for $T=1$ K and along the **c** axis for $T=0.25$ K.

$$I(T) \propto |T - T_N|^{2\beta}. \tag{12}$$

It was found that $\beta=0.30(1)$ for zero field, $\beta=0.35(1)$ for $\mu_0 H=7.25$ T, and $\beta=0.36(1)$ for $\mu_0 H=3$ T. Fits were performed over a reduced temperature of 0.2.

Figure 11 also shows two field scans: one scan with the field applied along the **c** axis and performed at 0.25 K, and a scan with the field applied along the **b** axis, performed at 1 K. The latter transition is unlike all other transitions discussed here, because here the field induces an ordered state starting from a paramagnetic state. The field scans are shown as a function of reduced field $|1-H/H_c|$. Power law fits were made using

$$I(H) \propto |H - H_c|^{2\beta} \tag{13}$$

in order to determine the critical exponents, and it was found that $\beta=0.400(1)$ for $T=0.25$ K and $\beta=0.481(3)$ for $T=1$ K. Fits were performed over the range 0.2 in reduced field.

For the temperature driven transition, the critical exponents β fall in the range 0.30–0.36 depending on the direction of the applied field, consistent with the critical exponents of the three-dimensional Ising universality class,[24] to which CDC belongs at zero field. For the field-induced transitions, the Ising character of the spin symmetry is enhanced due to the presence of uniform and perpendicular staggered fields. The critical exponents for the field-induced transitions, $\beta=0.400(1)$ and $\beta=0.481(3)$, are however higher than the critical exponent $\beta=0.325$ of the three-dimensional Ising universality class.

For an Ising quantum phase transition ($T=0$), the effective dimension of the quantum critical point is $D=d+z$ where $d=3$ is the spatial dimension and $z=1$ is the dynamical exponent. Since $D=4$ is the upper critical dimension, the quantum critical point is Gaussian (with logarithmic corrections) and $\beta=0.5$. Therefore, by measuring the field dependence of the order parameter at different temperatures, we expect to observe a crossover between the classical (finite T and $\beta=0.325$) and the quantum phase transitions ($T=0$ and $\beta=0.5$). This seems to be the natural explanation for the observed values of β close to 0.5. A similar increase in the apparent β critical exponent was observed in the singlet ground state system PHCC.[25]

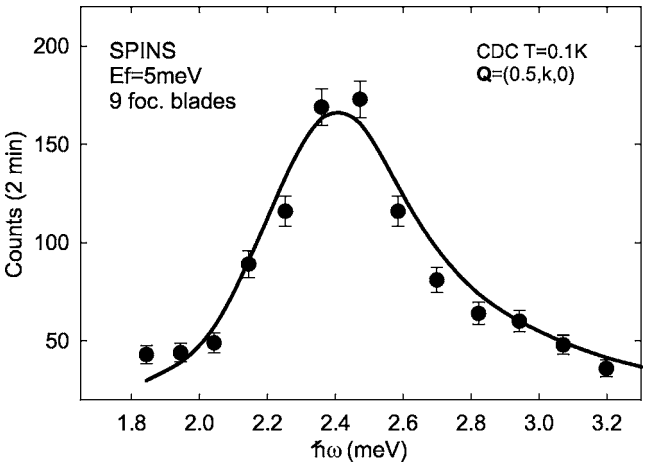

FIG. 12. Neutron scattering intensity as a function of energy transfer for zero field for $h=0.5$ measured using the SPINS spectrometer. The measurement was performed with nine analyzer blade channels set to reflect $E_f=5$ meV to the center of the detector. A Be filter rejected neutrons with energies higher than 5 meV from the detection system. The measurements were performed with the strongly dispersive direction along the scattered neutron direction, so that the measurements integrate neutron scattering over wave vectors along a weakly dispersive direction. The solid line represents the exact two-spinon cross section (Ref. 26) for $J=1.46(1)$ meV, convolved with the experimental resolution.

VI. INELASTIC NEUTRON SCATTERING

A. Exchange interactions

To characterize the Hamiltonian and accurately determine the strength of the spin interaction along the chain, we performed an energy scan for wave-vector transfer $\mathbf{Q}\cdot\mathbf{a}=\pi$ along the chain. At this wave vector the two-spinon spectrum characteristic of the AF $S=\frac{1}{2}$ chain should be concentrated over a small energy window and form a well-defined peak located at $\hbar\omega=\pi J/2$. Figure 12 shows that this is indeed the case, and that for CDC this well-defined excitation is located at $\hbar\omega=2.43(2)$ meV. A fit to the exact two-spinon cross section[26] convolved with the experimental resolution yields an excellent description of the observed spectrum, as shown in Fig. 12 for a value of intrachain exchange $J=1.46(1)$ meV. This value is very similar to that obtained from the temperature dependence of the magnetic susceptibility, which was 1.43 meV.[12]

B. Ground state energy at zero field and $\mu_0 H=11$ T

Inelastic neutron scattering not only allows determination of exchange constants, but also a measurement of the ground

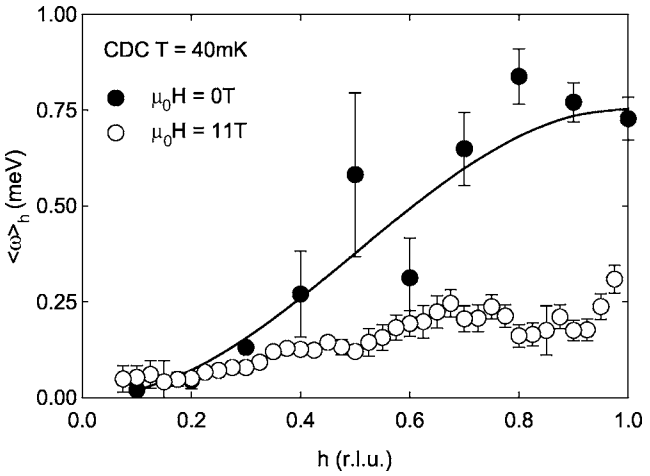

FIG. 13. First moment $\langle\tilde{\omega}\rangle_h=\hbar^2\int d\omega\omega I(h,\omega)$ of the well-defined excitations only as a function of wave vector h along the chain, for zero field and $\mu_0H=11$ T. The raw scattering data were corrected for a time-independent background measured at negative energy transfer, for monitor efficiency, and for the Cu^{2+} magnetic form factor, folded into the first Brillouin zone, and put onto an absolute scale using the elastic incoherent scattering from CDC.

state energy. The expectation value of the Hamiltonian, $\langle\mathcal{H}\rangle$, is proportional to the first moment of the dynamic structure factor, defined as $\langle\tilde{\omega}\rangle_{\mathbf{Q}}=\hbar^2\int d\omega\omega S(\mathbf{Q},\omega)$. Here the normalization of $S(\mathbf{Q},\omega)$ is chosen such that the total moment sum rule reads $\hbar\int S(\mathbf{Q},\omega)d\omega=S(S+1)/3$. So if the dynamic structure factor, $S(\mathbf{Q},\omega)$, is measured in absolute units, neutron scattering yields a measurement of $\langle\mathcal{H}\rangle$ as a function of field or temperature.

For a Heisenberg AF chain, the wave-vector dependence of $\langle\tilde{\omega}\rangle_h$ is given by

$$\langle\tilde{\omega}\rangle_h=-\tfrac{2}{3}\langle\mathcal{H}\rangle[1-\cos(\pi h)]. \tag{14}$$

We use this relation to describe the measured first moment, $\langle\tilde{\omega}\rangle_h$. Figure 13 shows that at zero field the experimental $\langle\tilde{\omega}\rangle_h$ follows this expression with $\langle\mathcal{H}\rangle=-0.4(1)J$, in excellent agreement with Bethe's result of $\langle\mathcal{H}\rangle\simeq-0.44J$ (Ref. 27). $\langle\tilde{\omega}\rangle_h$ was obtained by fitting the exact two-spinon cross section $S_{2sp}(\mathbf{Q},\omega)$ as calculated by Bougourzi *et al.*[26] to the data and computing $\langle\tilde{\omega}\rangle_h$ from the analytical expression for $S_{2sp}(\mathbf{Q},\omega)$.

Figure 13 shows the first moment $\langle\tilde{\omega}\rangle_h$ at $\mu_0H=11$ T including only contributions from sharp modes in the spectrum, thus excluding any contributions from continuum scattering. It was calculated by fitting a Gaussian to the experimentally observed peak in the energy spectra and by integrating the area under the Gaussian curve. $\langle\tilde{\omega}\rangle_h$ at $\mu_0H=11$ T is generally about 3 times smaller than $\langle\tilde{\omega}\rangle_h$ at zero field. This is evidence for the presence of substantial magnetic continuum scattering because both numerical and analytical calculations show that the first moments in an applied magnetic field should be larger than this measured value. This is based upon (A) numerical calculations[10] using the Lanczos method for finite chains of length between 12 and 24 spins which show that the ground state energy at $\mu_0H=11$ T for $H_{st}=0.075H$ is $\langle\mathcal{H}\rangle=-0.34J$, and (B) analytical calculations of the field dependence of the first moment which show that Eq. (14) acquires merely a small constant value with the application of uniform and staggered fields. Points (A) and (B) thus show that theoretically, only a slight depression of the first moment is expected upon application of magnetic fields.

Because our data presented in Fig. 13 include only resonant modes this result indicates that there are substantial contributions to the first moment from continuum scattering — perhaps not a surprise given that continuum scattering is the *sole* source of the first moment at zero field.

C. Comparison with the chains MF model

The magnetic order of weakly-coupled chains can be described by a chain mean-field theory developed by Schulz.[22] It gives the following relations between ordered magnetic moment m_0, T_N and the average of interchain interactions $|J'|$:[28,29]

$$|J'|=\frac{T_N}{0.78\sqrt{\ln\left(\frac{24.27J}{T_N}\right)+\frac{1}{2}-\ln\left[\ln\left(\frac{24.27J}{T_N}\right)\right]}} \tag{15}$$

$$m_0=0.295\ g\left[\frac{4|J'|}{J}\ln\left(\frac{2.585J}{4|J'|}\right)\right]^{1/2}. \tag{16}$$

The first relation allows an estimate for $|J'|$. In our case, where $T_N=0.93$ K and $J=1.5$ meV, this gives $|J'|=0.04$ meV. The real value for $|J'|$ may be somewhat higher because quantum fluctuations are not fully accounted for in the chain mean-field theory.

The second relation predicts the ordered moment for a Heisenberg chain magnet $m_0=0.38\mu_B$ for $|J'|=0.04$ meV and $g=2.14$, which is somewhat lower than the observed ordered moment even if one considers a higher value for $|J'|$ due to quantum fluctuations. The small difference may be due to interchain exchange interactions that are dominant along one spatial direction. Alternatively, the difference may be due to an Ising-type spin anisotropy which fixes the zero-field ordered moment along the **c** axis, thereby quenching quantum fluctuations and enhancing long-range order at low temperatures. Indeed, this term, no matter how small, induces long-range order even in the purely one-dimensional model at $T=0$ K.

VII. CONCLUSIONS

CDC is a rich model system in which to study quantum magnetism because an applied magnetic field leads first to a first-order phase transition and then to a high-field phase with soliton excitations via a quantum critical phase transition. In this paper, we characterized the material and its prox-

TABLE IV. Basis vectors of irreducible representations for the commensurate phase described with $\mathbf{k}=(0,0,0)$ for the Cu^{+2} sites. The components of the vector correspond to the spin component on the Cu sites in order given in (A1).

	ϕ^1	ϕ^2	ϕ^3	ϕ^4	ϕ^5	ϕ^6	ϕ^7	ϕ^8
$\mathbf{m}_1$	0	m_x	0	m_x	0	m_x	0	m_x
	m_y	0	m_y	0	m_y	0	m_y	0
	0	m_z	0	m_z	0	m_z	0	m_z
$\mathbf{m}_2$	0	m_x	0	$-m_x$	0	m_x	0	$-m_x$
	$-m_y$	0	m_y	0	$-m_y$	0	m_y	0
	0	$-m_z$	0	m_z	0	$-m_z$	0	m_z
$\mathbf{m}_3$	0	$-m_x$	0	m_x	0	m_x	0	$-m_x$
	$-m_y$	0	m_y	0	m_y	0	$-m_y$	0
	0	m_z	0	$-m_z$	0	$-m_z$	0	m_z
$\mathbf{m}_4$	0	$-m_x$	0	$-m_x$	0	m_x	0	m_x
	m_y	0	m_y	0	$-m_y$	0	$-m_y$	0
	0	$-m_z$	0	$-m_z$	0	m_z	0	m_z

imity to quantum criticality using specific heat and neutron scattering measurements. We determined the phase diagram as a function of temperature and field applied along all three crystallographic directions. The Bragg peak intensities and the temperature dependence of the specific heat demonstrate that when applying a field along the **a** and **c** axes, the spin system undergoes a quantum phase transition due to competing magnetic order parameters. Beyond the critical field, specific heat measurements show activated behavior typical for a gapped excitation spectrum. Theoretical analysis indicates that the spin gap results from spinon binding due to a staggered gyromagnetic factor and DM interactions. The gap energy was extracted from specific heat data using both a noninteracting boson model and an expression derived from a mapping of the Hamiltonian to the sine-Gordon model. We determined the strength of the staggered gyromagnetic factor and the DM interactions by analyzing the different field dependence of the gap for fields along the **a** and **c** axes. A magnetic field along the **c** axis leads to two phase transitions: a first-order spin-flop transition and a continuous phase transition at higher field to magnetic order described by only one irreducible representation. The continuous field driven quantum phase transition was characterized by an apparent critical exponent β, which is higher than expected for a classical phase transition in a three-dimensional antiferromagnet. The interpretation of this result is that the experiment probes a crossover regime affected by the $T=0$ quantum critical transition, which is above its upper critical dimension and therefore mean-field-like.

ACKNOWLEDGMENTS

The authors thank F. H. L. Essler, C. Landee, J. Copley, and I. Affleck for helpful discussions, and J. H. Chung for help during one of the experiments. Work at JHU was supported by the NSF through Grants Nos. DMR-9801742 and DMR-0306940. The DCS spectrometer and the high-field magnet at NIST were supported in part by the NSF through Grant Nos. DMR-0086210 and DMR-9704257. ORNL is managed for the US DOE by UT-Battelle Inc. under Contract No. DE-AC05-00OR2272. This work was also supported by the Swiss National Science Foundation under Contract No. PP002-102831.

APPENDIX A: DEFINITION OF THE MAGNETIC SUBLATTICE IN CDC

The unit cell contains four Cu^{2+} sites, which occupy the $4c$ position in the *Pnma* space group and are given by

$$\mathbf{r}_1 = (0.3209, 0.25, 0.3614),$$

$$\mathbf{r}_2 = (0.8209, 0.25, 0.1386),$$

$$\mathbf{r}_3 = (0.1791, 0.75, 0.8614),$$

$$\mathbf{r}_4 = (0.6791, 0.75, 0.6386). \quad \text{(A1)}$$

This numbering of the Cu^{2+} positions is used throughout the paper.

APPENDIX B: MAGNETIC GROUP THEORY ANALYSIS

Magnetic structures were inferred from diffraction data by considering only spin structures "allowed" by the space group and the given ordering wave vector $\mathbf{k}=(0,0,0)$. Landau theory of continuous phase transitions implies that a spin structure transforms according to an irreducible representation of the little group $G_{\mathbf{k}}$ of symmetry operations that leave the wave vectors $\mathbf{k}$ invariant. The eigenvectors ϕ^{λ} of the λth irreducible representations Γ^{λ} were determined using the projector method.[30] They are given by

$$\phi^{\lambda} = \sum_{g} \chi^{\lambda}(g) g(\phi), \tag{B1}$$

where g is an element of the little group and ϕ is any vector of the order parameter space. $\chi^{\lambda}(g)$ is the character of symmetry element g in representation Γ^{λ}.

We start by considering the symmetry elements of the *Pmna* space group of CDC

$$\{1, \bar{1}, 2_x, 2_y, 2_z, m_{xy}, m_{xz}, m_{yz}\}. \tag{B2}$$

Here 1 is the identity operator, $\bar{1}$ is inversion at the origin, 2_{α} denotes a 180° screw axis along the crystallographic direction $\alpha = a$, b or c (180° rotation operation followed by a translation). $m_{\alpha\beta}$ is a glide plane containing axes α and β. The group is nonsymmorphic because the group elements $\{R|\mathbf{a}\}$ consist of an operation R followed by a translation $\mathbf{a}$ equal to one-half a direct lattice vector.

The ordering wave vector $\mathbf{k} = (0,0,0)$ is invariant under all operations of the space group, so the little group $G_{\mathbf{k}}$ equals the space group. The group consists of eight different classes and therefore has eight irreducible representations. The irreducible representations and their basis vectors are given in Table IV. The magnetic representation can be written as

$$\Gamma^{k} = \Gamma^{1} \oplus 2\Gamma^{2} \oplus \Gamma^{3} \oplus 2\Gamma^{4} \oplus \Gamma^{5} \oplus 2\Gamma^{6} \oplus \Gamma^{7} \oplus 2\Gamma^{8}. \tag{B3}$$

The low-temperature magnetic structure was inferred from the integrated intensities of rocking scans through magnetic Bragg peaks in the $(h,k,0)$ plane. An absolute scale for the integrated intensities of these reflections was obtained from measurements of nuclear Bragg peaks. The magnetic structure factors squared were obtained after correcting for resolution effects, the sample mosaic, and the magnetic form factor of the Cu^{2+} ions.

[1] F. D. M. Haldane and M. R. Zirnbauer, Phys. Rev. Lett. **71**, 4055 (1993).
[2] J. C. Talstra and F. D. M. Haldane, Phys. Rev. B **50**, 6889 (1994).
[3] S. Sachdev, *Quantum Phase Transitions* (Cambridge University Press, Cambridge, 1999).
[4] M. B. Stone, D. H. Reich, C. Broholm, K. Lefmann, C. Rischel, C. P. Landee, and M. M. Turnbull, Phys. Rev. Lett. **91**, 037205 (2003).
[5] G. Müller, H. Thomas, H. Beck, and J. C. Bonner, Phys. Rev. B **24**, 1429 (1981).
[6] D. C. Dender, P. R. Hammar, D. H. Reich, C. Broholm, and G. Aeppli, Phys. Rev. Lett. **79**, 1750 (1997).
[7] R. Feyerherm, S. Abens, D. Gunther, T. Ishida, M. Meissner, M. Meschke, T. Nogami, and M. Steiner, J. Phys.: Condens. Matter **12**, 8495 (2000).
[8] M. Oshikawa, K. Ueda, H. Aoki, A. Ochiai, and M. Kohgi, J. Phys. Soc. Jpn. **68**, 3181 (1999).
[9] M. Kenzelmann, Y. Chen, C. Broholm, D. H. Reich, and Y. Qiu, Phys. Rev. Lett. **93**, 017204 (2004).
[10] M. Kenzelmann, C. D. Batista, Y. Chen, C. Broholm, D. H. Reich, S. Park, and Y. Qiu, Phys. Rev. B **71**, 094411 (2005).
[11] R. D. Willett and K. Chang, Inorg. Chim. Acta **4**, 447 (1970).
[12] C. P. Landee, A. C. Lamas, R. E. Greeney, and K. G. Bücher, Phys. Rev. B **35**, 228 (1987).
[13] I. Dzyaloshinskii, J. Phys. Chem. Solids **4**, 241 (1958).
[14] T. Moriya, Phys. Rev. **120**, 91 (1960).
[15] M. Oshikawa and I. Affleck, Phys. Rev. Lett. **79**, 2883 (1997).
[16] R. F. Flipsen, Masters thesis, University of Eindhoven, 1983.
[17] M. Troyer, H. Tsunetsugu, and D. Würtz, Phys. Rev. B **50**, 13515 (1994).
[18] R. F. Dashen, B. Hasslacher, and A. Neveu, Phys. Rev. D **11**, 3424 (1975).
[19] I. Affleck and M. Oshikawa, Phys. Rev. B **60**, 1038 (1999).
[20] F. H. L. Essler and A. M. Tsvelik, Phys. Rev. B **57**, 10592 (1998).
[21] F. H. L. Essler, Phys. Rev. B **59**, 14376 (1999).
[22] H. J. Schulz, Phys. Rev. Lett. **77**, 2790 (1996).
[23] M. Sato and M. Oshikawa, Phys. Rev. B **69**, 054406 (2004).
[24] J. C. LeGuillou and J. Zinn-Justin, Phys. Rev. B **21**, 3976 (1980).
[25] M. B. Stone, C. Broholm, D. H. Reich, O. Tchernyshyov, P. Vorderwisch, and N. Harrison, Phys. Rev. Lett. **96**, 257203 (2006).
[26] A. H. Bougourzi, M. Karbach, and G. Müller, Phys. Rev. B **57**, 11429 (1998).
[27] H. A. Bethe, Z. Phys. **71**, 205 (1931).
[28] M. Bocquet, Phys. Rev. B **65**, 184415 (2002).
[29] A. Zheludev, S. Raymond, L.-P. Regnault, F. H. L. Essler, K. Kakurai, T. Masuda, and K. Uchinokura, Phys. Rev. B **67**, 134406 (2003).
[30] V. Heine, *Group Theory in Quantum Mechanics* (Dover, New York, 1993), pp. 119 and 288.